



Originally published as:

Pick, L., Lombardo, V., Zaksek, K. (2018): Assessment of the Dual-Band method by an indoor analog experiment. - *Annals of Geophysics*, 61.

DOI: <http://doi.org/10.4401/ag-7791>



**ACCEPTED ON ANNALS OF GEOPHYSICS, 61, 2018; Doi:
10.4401/ag-7791**

Assessment of the Dual-Band method by an indoor analog experiment

**Leonie Pick, University of Hamburg, Hamburg (GER); now at GFZ German
Research Centre for Geosciences, Potsdam (GER)**

**Valerio Lombardo, National Institute of Geophysics and Volcanology, Rome
(IT)**

**Klemen Zaksek, University of Hamburg, Hamburg (GER); now at University of
Ljubljana, Ljubljana (SLO)**

Title:

Assessment of the Dual-Band method by an indoor analog experiment

5 Authors:

Leonie Pick, University of Hamburg, Hamburg (GER); now at GFZ German Research Centre for Geosciences, Potsdam (GER)

10 Valerio Lombardo, National Institute of Geophysics and Volcanology, Rome (IT)

Klemen Zakšek, University of Hamburg, Hamburg (GER); now at University of Ljubljana, Ljubljana (SLO)

15 Correspondence:

klemen.zaksek.geo@gmail.com

Paper Type: Fast Track

Abstract:

20 The evaluation of infrared satellite images over active lava flows assists the identification of potentially threatened areas and thereby the overall lava inundation hazard assessment. The estimation of the lava flow's size and temperature is not trivial as the lava occupies only a small fraction ($< 1\%$) of a typically resolved target pixel (e.g. from Landsat 7-ETM+; EOS-MODIS). Conventionally, this is solved by processing observations in at least two separate infrared spectral wavebands. We investigate the resolution limits of the Dual-Band (DB) method by means of a uniquely designed indoor analog experiment. A volcanic thermal anomaly is simulated by an electrical heating alloy of 0.5 mm diameter installed on a plywood panel. Satellite observations are simulated by two thermographic cameras with wavebands comparable to those available from satellite data. 40 These range from the short-wave infrared (SWIR) over the mid-wave infrared (MIR) to the thermal infrared (TIR). In the conducted experiment, the hotspot's pixel fraction (p) was successively reduced by increasing the camera-to-target distance from 2 m ($p = 41.7\%$) to 38 m ($p = 2.2\%$). We carried out three experiments with different wire temperatures and compare different DB setups. In the case of the hottest wire (1019 K), 50 the standard method gives relative deviations between the observed and theoretical hotspot

area fractions below 16 % for about one third of the cases (i.e. distances).

55 1. Introduction

The discipline of satellite thermal remote sensing provides physical insight into the processes governing volcanic activity and has become a valuable tool of volcanology since the pioneering paper on the topic was published (Gawarecki et al., 1965). The volcanological community is confronted with the problem, that none of the currently operational satellite 60 sensors have been designed primarily for volcanological purposes. Consequently, the available data, mostly from meteorological satellites, is not ideal for volcano surveillance in two basic regards. First, the characteristics of the spectroradiometers themselves, essentially the three resolutions in the spatial, spectral, and radiometric domain are not optimally balanced. Secondly, the satellite orbits are not well adapted, affecting the satellite-volcano 75 viewing geometry and temporal resolution. Apart from these data limitations, there is the general difficulty that the radiance measured by the sensor differs from the radiance emitted by the ground heat source, mainly due to surface emissivity, atmospheric and geometric influences. 80

To derive higher-level estimates of volcanic activity, such as lava discharge rate (Harris et al., 2005; Calvari et al., 2010), the flow's area and temperature have to be estimated first, usually using the so called Dual-Band (DB) method (Dozier, 1981). This method allows thermal un-mixing of a pixel composed of two temperature components (Crisp and 90 Baloga, 1990; Dozier, 1981; Rothery et al., 1988): 1) a hot component with temperature T_H covering the pixel fraction p , and 2) a background component with temperature T_B covering the pixel fraction $1-p$. With sensors of coarse spatial resolution (e.g. Moderate Resolution Imaging Spectroradiometer – MODIS, Advanced Very High Resolution Radiometer – AVHRR) this is an unrealistic assumption, as each pixel might consist of several further components with different thermal properties, rendering an error of more than 100 K in T_H (Oppenheimer, 1993; Mougini-Mark et al., 1994; Wright et al., 2000;

Lombardo and Buongiorno, 2006; Vaughan et al., 2010, Zakšek et al., 2013).

The influence of the interplay between all these components on the results of the DB method is still difficult to estimate. Here, we focus on the influence of the fractional area of an anomaly within a pixel (p). To systematically examine this effect, it needs to be isolated from the other influences. For this purpose, the satellites' measurement situation is simulated in an experiment, using a steady heat source, which is observed by thermal cameras in spectra commonly found for satellite sensors.

2. Experiment

2.1 The Lava Simulator

The following list summarizes requirements for the simulated heat source:

- Target should be a two component mixed pixel with a hot component of at least $T_H = 600$ K comparable to crusted lava (Lombardo et al., 2012) and a background component of significantly lower temperature $T_B \approx 330$ K.
- Target should be mobile to allow different camera-to-target distances and thereby different pixel sizes.
- Hot component's area percentage (p) should ultimately be comparable to those from satellite measurements, being $\approx 1\%$.
- Temperatures should be constant during the measurement campaign.
- Influences of the target's surroundings should be minimized.

The "Lava Simulator's" heat source is a single heating wire alloy (Fig. 1). Electricity is converted into heat through Joule heating, with the heating power depending on the electrical current and the resistivity. Considering different materials, we decided to use an alloy with a 0.5 mm diameter made of Isachrom 60 (NiCr6015) because of its high specific electrical resistivity and oxidation resistance. A laboratory power supply unit is used as a power source with a total maximal output of 400 W.

2.2 Experimental setup

The pixel fraction p occupied by the hot wire decreases with increasing distance between the cameras and the Lava Simulator. The Simulator is seated on a trolley, that is pushed away from the cameras in a 40 m long hallway. The distance between the cameras and the Lava Simulator was increased by 2 m at each step, with the closest measurement at a distance of 2 m ($p = 41.7\%$) and the furthest at 38 m ($p = 2.2\%$). At each step, we recorded mean temperatures of 10 s lasting observations with two cameras, producing a SWIR, MIR and TIR image. The experiment was repeated three times, each time with a different temperature of the alloy, i.e. amperage of the power supply. We call the runs LOW (small T_H), MED (medium T_H) and HOT (large T_H).

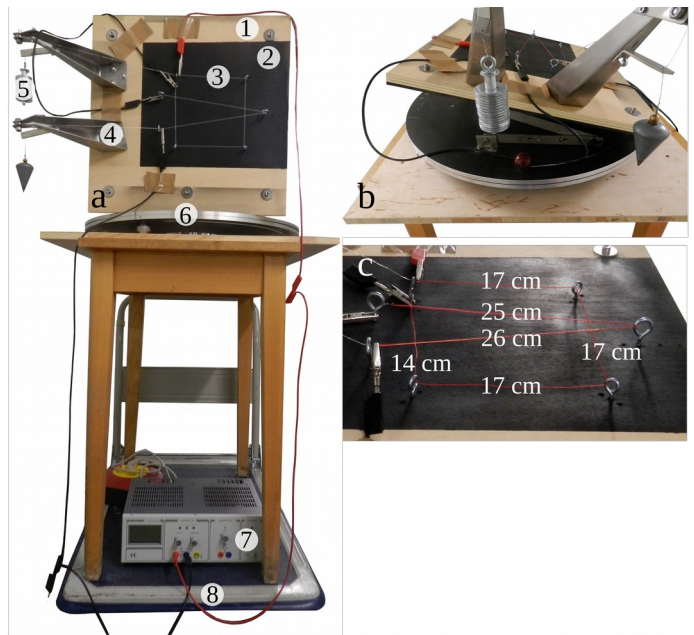


Fig. 1. Lava Simulator setup. **a:** Front view. 1) 50 cm \times 50 cm plywood panel, 2) high emissivity (0.95) area colored with Senotherm spray, 3) Isachrom 60 alloy, 4) tensioning mechanism, 5) weights to support alloy tensioning, 6) revolvable and tiltable base, 7) electrical supply unit, 8) trolley. **b:** Side view. **c:** Close-up of heated alloy.

2.3 Cameras

We used two different cameras of the company Infratec. VarioCam (VC) operates mainly in the thermal infrared spectrum (TIR; centered at $10.3 \mu\text{m}$). ImageIR 8300 (IR) is equipped with two filters covering the short-wave (SWIR; centered at $2.36 \mu\text{m}$) and

mid-wave infrared (MIR; centered at 3.90 μm) spectra. In both cameras, the detector elements are arranged in a Focal Plane Array, including 640×480 (VC) or 640×512 (IR) single detectors. VC has a lens with 30 mm focal length (angle resolution 0.8 mrad) and IR has a lens with 25 mm focal length (angle resolution 0.6 mrad). Both cameras provide observations with 1 % accuracy. The cameras are fixed on a tripod by custom-made housing in order to keep the viewing directions parallel.

3. Methods

3.1 SWIR emissivity estimation

The temperature observations require an accurate determination of the emissivities of the emitting surfaces. Thus, in a dark-room environment, we collected spectra from the operating Lava Simulator using the field-portable Spectroradiometer ASD FieldSpec Pro (FS). FS is composed of three spectrometers which measure the spectral radiation energy in different portions of the wavelength spectrum from 0.35 to 2.5 μm with a spectral resolution of 2–12 nm.

The electromagnetic radiation emitted from the surface is collected by the instrument entry optics and projected into a holographic diffraction grating. FS is provided with a bare fiber optic and a conical field of view (FOV) of 35°. However, the bare fiber FOV has been further reduced using alternative fore optic tubes of 1° and 3°.

Given the temperature heterogeneities observed by the Lava Simulator, a new algorithm has been developed to take into account the radiance contributions from surfaces radiating at different temperatures. We assume a two thermal components model for the Lava Simulator. The radiance R detected by FS at wavelength λ is the average of the radiances emitted by the hot (at T_H) and cold (at T_B) surfaces, weighted by their corresponding pixel fractions:

$$R(T_i, \lambda) = \varepsilon(\lambda) [p \cdot R(T_H, \lambda) + (1 - p) \cdot R(T_B, \lambda)] \quad (1)$$

R is the radiance of a blackbody at temperature T and wavelength λ according to Planck's Law, T_i is the integrated temperature and $\varepsilon(\lambda)$ is the spectral emissivity. The Drap-

ing algorithm allows the simultaneous estimation of T_H , T_B , p , and $\varepsilon(\lambda)$ through the following steps:

- Identification of the maximum measured radiance $R_{\max} = \max[R(\lambda)]$ across all wavelengths.
- Creation of a lookup table of spectra derived from Eq. 1. Only spectra respecting the condition $R(T_i, \lambda) \geq R_{\max}$ are considered. This guarantees that $\varepsilon(\lambda) \leq 1$.
- Calculation of the Spearman rank correlation coefficient (ρ) between the measured radiances and each spectrum of the lookup table.
- Maximum ρ identifies the spectrum $R(T_i, \lambda)$ derived from Eq. 1 that best matches the measured radiances $R(\lambda)$ and therefore fixes the parameter triplet T_H , T_B , p of the underlying two thermal components model.
- Spectral emissivity:

$$\varepsilon(\lambda) = R(\lambda)/R(T_i, \lambda) \quad (2)$$

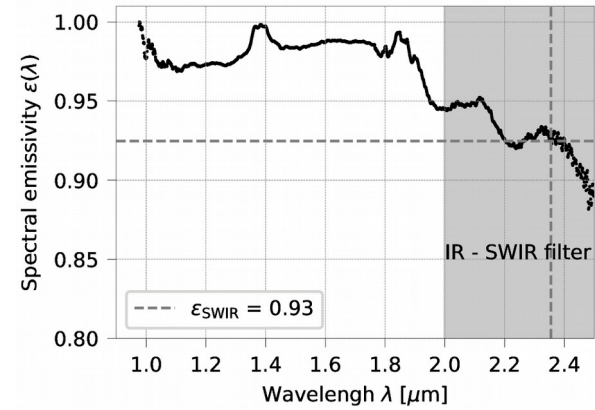


Fig. 2. Spectral emissivity of the hot wire derived with the Draping algorithm. Gray area: SWIR filter of IR camera. Dashed lines: Emissivity (0.93) at filter's central wavelength (2.36 μm).

Figure 2 shows the emissivity spectrum derived from the radiance measurements. The emissivity is seen to be 0.93 at the central wavelength of IR's SWIR filter (dashed lines). The iterative method (section 3.2) gives a very similar value of 0.95. We keep the latter value to account for the fact that the Draping algorithm determines a lower bound of the SWIR emissivity as well as ensuring consistency with the emissivity calculations in MIR and TIR.

3.2 MIR and TIR emissivity calculation

As we had emissivity observations available only for the SWIR spectrum, we had to determine the emissivity of the metal alloy in the MIR and TIR differently. We carried out an iterative procedure based on the camera observations from all distances.

First, we estimated the theoretical anomalous pixel fraction p_{theo} as a function of the distance between the Lava Simulator and the cameras, see Fig. 3a. Then, we performed various runs of the DB method using our SWIR and MIR camera observations to calculate p (and T_H , see section 4.1). For these runs, we set the SWIR emissivity to be constant (0.95, see section 3.1) and varied the MIR emissivity between zero and one in steps of 0.05. A MIR emissivity of 0.85 gave the p -solution with the smallest cumulative deviation from p_{theo} across all distances and was finally chosen. We performed the same procedure for SWIR and TIR camera observations, which resulted in an emissivity of 0.25 for the alloy in the TIR. The emissivity of the sprayed background (black, see Fig. 1) was set to 0.95 for all wavelengths, following the Senotherm spray specifications.

4. Results

4.1 DB method: T_B is known

DB needs two observations and one assumption to solve a system with three variables. Typically, one assumes a background temperature T_B and solves for the temperature of the anomaly T_H and its fraction p ("standard method"). With three independent observations (section 2.2), we can produce different solutions, shown in Fig. 3 for the HOT setup. Overall, the solutions involving SWIR observations are most accurate with regard to the Root Mean Squared Error (RMSE) (panel a). The smallest relative error in p of $\sim 1\%$ is reached by the MIR-SWIR combination at a distance of 16 m ($p = 5.2\%$). At the max. distance of 38 m ($p = 2.2\%$), the MIR-SWIR solution gives a relative error of 28.7%. Calculated T_H values vary notably around their means (panel b) with a minimum RMSE of 96.1 K for the MIR-SWIR combination. They seem to converge only at distances ≥ 26 m ($p = 3.2\%$).

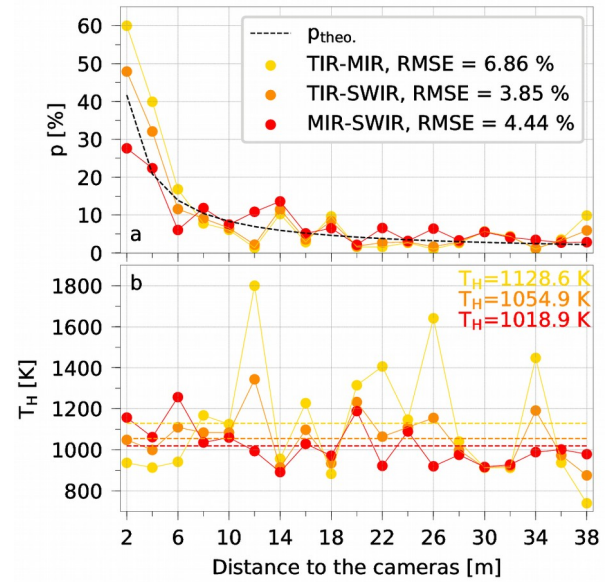


Fig. 3. Solution of the DB method (**a:** pixel fraction p , **b:** T_H) for the HOT setup and three band combinations with assumed $T_B = 370$ K. Dashed lines indicate the expected values for p (known) and T_H (mean of solutions over distances, values annotated).

4.2 DB method: p is known

Our experimental setup allows to evaluate a less common variation of the DB method ("assumed p method"). We provide the theoretical hot pixel fraction p (Fig. 3a, black) and estimate T_H and T_B .

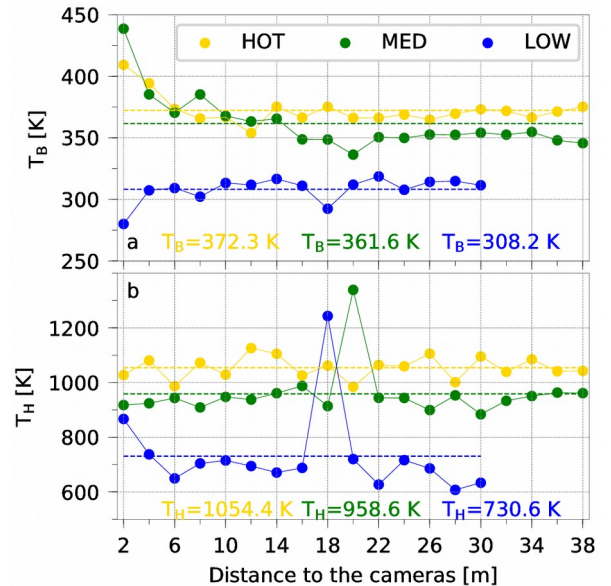


Fig. 4. Solution of the DB method (**a:** T_B and **b:** T_H) for the TIR-MIR band combination and three runs of the experiment with given pixel fraction p . Dashed lines indicate the mean values for T_B and T_H (annotated).

Figure 4 shows the solutions for the experimental setups HOT, MED & LOW using the TIR-MIR band combination, most sensitive to low temperatures (i.e. T_B). The background temperature is most robustly determined for the HOT setup ($T_B = 372$ K, RMSE = 9.7 K, panel a). Variations originate primarily from close distances ≤ 6 m ($p = 13.9\%$), beyond which the results converge towards the mean (dashed). The variability in T_H is remarkably reduced compared to the results of the standard method. HOT gives $T_H = 1054$ K and the lowest RMSE = 39.2 K, while the runs with lower wire temperatures give RMSEs more than twice as large due to one outlier in MED and two in LOW (noisiest, panel b).

4.3 Tri-Band method: no assumptions

According to Fig. 4a, the assumption of a constant background temperature may result in significant errors. A better solution for the two thermal components case can be achieved by using the observations of all three wavebands (Flynn et al., 1994). Then, no assumption is needed and p , T_H and T_B are simultaneously estimated (Fig. 5).

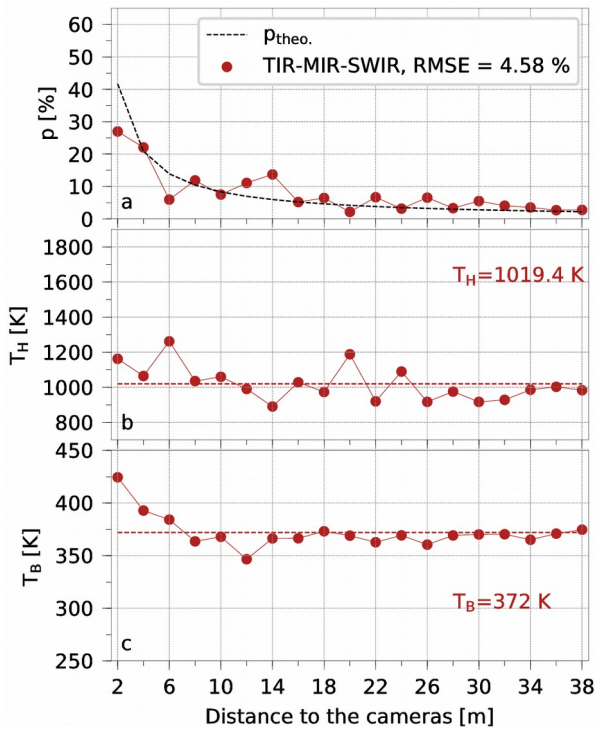


Fig. 5. Solution of the DB method for the HOT setup (**a**: p , **b**: T_H , and **c**: T_B). Dashed lines indicate the expected values for p (known), T_H and T_B (mean of solutions over distances, values annotated).

The RMSEs for p (panel a) and T_H (97.4 K) are negligibly larger than those of the SWIR solutions using the standard method (Fig. 3, orange & red). However, improvements compared to the standard method are registered: First, the smallest relative error in p has reduced to 0.6 % at 16 m. Secondly, the relative errors at 38 m, the case most relevant for satellite thermal remote sensing, have decreased to 24.9% for p and 3.6% for T_H . The mean of T_B (372 K) is in excellent agreement with that calculated by the best assumed p method (see Fig. 4a, yellow). Likewise, the mean of T_H (1019 K) agrees well with that given by the best standard method (see Fig. 3b, red).

5. Discussion

Overall, the presented solutions obtained by the different methods are coherent, lending support to the serviceability of the experimental setup and the relevance of the results. Subpixel characterization techniques are pivotal in remote sensing of active lava flows. Although the reliability of the DB method has frequently been challenged in this context (e.g. Wright et al., 2003; Harris, 2013), it is still widely used until today (e.g. Aufaristama et al., 2018) due to the lack of satellite sensors with multiple infrared channels across the spectrum.

To our knowledge this study is the first that systematically evaluates the dependence of the DB method on the hot pixel fraction p under “controlled” measurement conditions. It complements studies that test the DB method using synthetic data, as in Murphy et al. (2014). The authors calculate synthetic radiance spectra in the SWIR from two thermal components pixel and conclude that DB is statistically incapable of reliably, i.e. with 95% confidence, constraining p , T_H or T_B (deviations $\geq 11\%$). In our experiment, we use different infrared wavelength bands and succeed in estimating p with deviations down to $\sim 1\%$ (MIR-SWIR, Fig. 3a). However, the standard DB method (assumed T_B) will likely result in large p deviations ($\geq 29\%$) for small pixel fractions ($\leq 2.2\%$). Best results are obtained by using SWIR observations, for which we determined a reliable wire

emissivity of 0.95. The iteratively estimated emissivities in TIR (0.25) and MIR (0.85) are smaller and relatively uncertain, as they were not validated independently based on spectrometer measurements (section 3.1). The TIR-MIR combination thus gives the least accurate p results. They can not be transferred to an active lava flow, for which one would expect a far greater emissivity above 0.9 across the infrared spectrum. A higher accuracy of the p estimate can be achieved if observations in TIR, MIR and SWIR wavebands are available (Fig. 5a), as for instance at Visible Infrared Imaging Radiometer Suite (VIIRS). However, the spatial resolution of VIIRS may be considered as too coarse. A preferable option is HypsIRI mission scheduled for launch in 2022. Meanwhile, the fusion of high resolution optical data with that from thermal sensors can boost the accuracy of the fractional area estimate.

Subpixel temperatures T_H and T_B can be calculated most robustly (RMSEs 10 K, 40 K) if p is known (Fig. 4). Such a measurement setup is provided today by numerous high resolution satellite data (e.g. Sentinel 1 and 2, GeoEye, WorldView, Planet). Their integration in a standard workflow based on, e.g., MODIS data can significantly increase the quality of the results.

The DB method operates best in the case of hot anomalies (Fig. 4). A sensor similar to the Advanced Spaceborne Thermal Emission and Reflection Radiometer – ASTER (with an additional MIR band) or FireBIRD (Zakšek et al., 2015; with an additional SWIR band) is therefore desirable in terms of DB method accuracy.

6. Conclusions

We implemented a simulation environment for the quantitative estimation of subpixel sizes and temperatures. It is important to understand quantitative relationships between instrumental spectral and radiometric characteristics and data exploitable for lava flow subpixel features. Our analyses show that the standard DB method leads to a large percent deviation of ~29 % for small p (2.2%). This can be mitigated by

- using MIR, SWIR and TIR wavebands simultaneously. This confirms simulations by Lombardo et al. (2012), stating that observations in three appropriate, independent spectral bands are necessary to obtain reliable solutions.
- a more accurate determination of surface emissivities, possibly using a spectral library approach (Murphy et al., 2014).
- the fusion of thermal data with high-resolution optical / radar data.
- additional SWIR and MIR sensors.

The above points suggest improvements in future payload development regarding the dynamic range and band wavelengths.

Acknowledgments

This research has been supported by a grant from the German Science Foundation (DFG), number ZA659/1-1. We would like to thank Joachim Bülow and Thomas Schön for supporting the construction of the Lava Simulator as well as Matthias Hort for his valuable comments regarding the design of the whole experiment.

References

- Aufaristama, M., Hoskuldsson, A., Jonsdottir, I., Ulfarsson, M.O., Thordarson, T., 2018. New Insights for Detecting and Deriving Thermal Properties of Lava Flow Using Infrared Satellite during 2014–2015 Effusive Eruption at Holuhraun, Iceland. *Remote Sens.* 10(1), 151. <https://doi.org/10.3390/rs10010151>
- Calvari, S., Lodato, L., Steffke, A., Cristaldi, A., Harris, A.J.L., Spampinato, L., Boschi, E., 2010. The 2007 Stromboli eruption: Event chronology and effusion rates using thermal infrared data. *J. Geophys. Res. Solid Earth* 115, B04201. <https://doi.org/10.1029/2009JB006478>
- Crisp, J., Baloga, S., 1990. Estimating eruption rates of planetary lava flows. *Icarus* 85, 512–515. [https://doi.org/10.1016/0019-1035\(90\)90129-W](https://doi.org/10.1016/0019-1035(90)90129-W)
- Dozier, J., 1981. A method for satellite identification of surface temperature fields of

- subpixel resolution. *Remote Sens. Environ.* 11, 221–229. [https://doi.org/10.1016/0034-4257\(81\)90021-3](https://doi.org/10.1016/0034-4257(81)90021-3)
- 545 Flynn, L.P., Mougini-Mark, P.J., Horton, K.A., 1994. Distribution of thermal areas on an active lava flow field: Landsat observations of Kilauea, Hawaii, July 1991. *Bull. Volcanol.* 56 (4), 284–296.
- 550 Gawarecki, S.J., Lyon, R.J.P., Nordberg, W., 1965. Infrared spectral returns and imagery of the Earth from space and their application to geological problems: scientific experiments for manned orbital flight. *Am. Astronaut. Soc. Sci. Technol. Ser.* 4, 13–133.
- 555 Harris, A., 2013. *Thermal Remote Sensing of Active Volcanoes: A User's Manual*. Cambridge University Press. ISBN: 9780521859455.
- 560 Harris, A., Dehn, J., Patrick, M., Calvari, S., Ripepe, M., Lodato, L., 2005. Lava effusion rates from hand-held thermal infrared imagery: An example from the June 2003 effusive activity at Stromboli. *Bull. Volcanol.* 68, 107–117. <https://doi.org/10.1007/s00445-005-0425-7>
- 565 Lombardo, V., Buongiorno, M.F., 2006. Lava flow thermal analysis using three infrared bands of remote-sensing imagery: A study case from Mount Etna 2001 eruption. *Remote Sens. Environ.* 101, 141–149. <https://doi.org/10.1016/j.rse.2005.12.008>
- 570 Lombardo, V., Musacchio, M., Buongiorno, M.F., 2012. Error analysis of subpixel lava temperature measurements using infrared remotely sensed data. *Geophys. J. Int.* 191, 112–125. <https://doi.org/10.1111/j.1365-246X.2012.05632.x>
- 575 Mougini-Mark, P.J., Garbeil, H., Flament, P., 1994. Effects of viewing geometry on AVHRR observations of volcanic thermal anomalies. *Remote Sens. Environ.* 48, 51–60. [https://doi.org/10.1016/0034-4257\(94\)90113-9](https://doi.org/10.1016/0034-4257(94)90113-9)
- 580 Murphy S.W., Oppenheimer, C., Souza Filho, C.R., 2014. Calculating radiant flux from thermally mixed pixels using a spectral library. *Remote Sens. Environ.* 142, 83–94. <https://doi.org/10.1016/j.rse.2013.11.010>
- 585 Oppenheimer, C., 1993. Thermal distributions of hot volcanic surfaces constrained using three infrared bands of remote sensing data. *Geophys. Res. Lett.* 20, 431–434. <https://doi.org/10.1029/93GL00500>
- 590 Rothery, D.A., Francis, P.W., Wood, C.A., 1988. Volcano monitoring using short wavelength infrared data from satellites. *J. Geophys. Res.* 93, 7993–8008.
- 600 Vaughan, R.G., Keszthelyi, L.P., Davies, A.G., Schneider, D.J., Jaworowski, C., Heasler, H., 2010. Exploring the limits of identifying sub-pixel thermal features using ASTER TIR data. *J. Volcanol. Geotherm. Res.* 189, 225–237. <https://doi.org/10.1016/j.jvolgeores.2009.11.010>
- 605 Wright, R., Flynn, L.P., 2003. On the retrieval of lava-flow surface temperatures from infrared satellite data. *Geology* 31, 893–896. <https://doi.org/10.1130/G19645.1>
- 610 Wright, R., Rothery, D.A., Blake, S., Pieri, D.C., 2000. Improved remote sensing estimates of lava flow cooling: A case study of the 1991–1993 Mount Etna eruption. *J. Geophys. Res.* 105, 23681–23694. <https://doi.org/10.1029/2000JB.900225>
- 615 Zakšek, K., Shirzaei, M., Hort, M., 2013. Constraining the uncertainties of volcano thermal anomaly monitoring using a Kalman filter technique. *Geol. Soc. Lond. Spec. Publ.* 380, 137–160. <https://doi.org/10.1144/SP380.5>
- 620 Zakšek, K., Hort, M., Eckehard, L., 2015. Satellite and Ground Based Thermal Observation of the 2014 Effusive Eruption at Stromboli Volcano. *Remote Sens.* 7(12), 17190–17211. <http://doi.org/10.3390/rs/71215876>.
- 625 630